Astron. Astrophys. 355, 155–164 (2000)

ASTRONOMY AND ASTROPHYSICS

17 μm imaging of η Carinae: an onion-like structure for the lobes?⋆

E. Pantin[1,2,3] **and D. Le Mignant**[1,4]

[1] European Southern Observatory, Santiago, Chile
[2] Katholieke Universiteit, Leuven, Belgium
[3] DSM/DAPNIA/SAp CE Saclay, France
[4] Laboratoire d'Astrophysique de l'Observatoire de Grenoble, France

Received 15 January 1999 / Accepted 22 July 1999

Abstract. We have obtained a 17 μm image of the η Carinae nebula with a signal to noise ratio never reached before. Once deconvolved, the spatial resolution is of the order of 0.5″. The ring and arclike structures seen at 17 μm are very similar to those observed at 12.5 μm; however the intensity maximum is located elsewhere in a dense cold structure seemingly torus-like around the central object. The high S/N ratio achieved in the image gives us a 2-D photometry map of the nebula at 17 μm with a good precision.

Combined with a simultaneous N band (10 μm) image, and a model of the dust thermal emission, we have built up a colour temperature map, which is then used to construct a map of the dust column density in the lobes.

We could test the different models found in the literature concerning the radial density of matter in the lobes, and specifically, pay attention to the question of the hollowness of the lobes. Our modeling of the SE lobe shows that it has a more complex structure than just an external shell, as claimed in some previous works. Our observations can be fit by a radial density model which includes a main, thick, external shell, a secondary shell between 0.30 and 0.55 times the lobe radius, and some material at the center of the lobe. The external shell is believed to be associated with the 1842 Greater Eruption, but we still lack 3D kinematic constrains to assess that the secondary shell is due to the 1890 Lesser Eruption.

Key words: infrared: stars – ISM: structure – ISM: dust, extinction – stars: variables: general – book reviews – radiation mechanisms: thermal

1. Introduction

The star η Carinae and its surrounding nebula is a fascinating object that is thought to be a luminous blue variable (LBV) star that has ejected large amounts of material during violent eruption stages, creating the bipolar nebula seen today called the Homunculus. It has been the subject of many recent studies, including Hubble Space Telescope observations (Davidson et al. 1997; Currie et al. 1996b) and near-infrared observations with adaptive optics (Rigaut & Gehring 1995). However, the mechanism required to form the two gigantic lobes of gas and dust seen today remains poorly understood, although it is relatively well established that the Homunculus was formed during a massive eruption of the star in 1837-1847 (Gaviola 1950). An important question regarding the physical models to interpret the formation of the Homunculus is the geometry and radial density of gas and dust in the lobes. Many previous investigators have addressed this question. Recently, Currie et al. (1996a) interpreted their HST WFPC2 doppler imaging data using a bipolar "double-flask" model. Meaburn et al. (1993), concluded from spectropolarimetric observations that the polarisation profiles can be modeled by silicate grains in the walls of two hollow cavities. Allen & Hillier (1993), argued for a bipolar or twin-bubble structure from spectroscopic observations in the visible. Hackwell et al. (1986), found, using a six-channel mid-infrared bolometer mapping plus maximum entropy enhancement (final resolution 0.8″), that the dust is clumpy and distributed in bipolar horns. Smith et al. (1995) got 12.5 μm images of the nebula and estimated the external shell to have a radius of 1/4 of the lobe radius. On the approximation of being spherical shells and the interior filling being uniform, they found that the lobes cannot be completely hollow, but would be filled with an inner density three or four times lower than that in the shells. They also got images of the nebula at 17 μm but with an evident lack of sensitivity, as shown on Fig. 3 of Smith et al. (1995), preventing them neither to provide an accurate photometry of η Carinae (50% of error) nor deconvolve these data. Aitken et al. (1995) studied the grain alignment properties from 12.5 μm polarimetric imaging. In particular, they found that the polarisation peaks at the projected boundaries of the lobes rather than peaking near the projected centers of the lobes (case of strictly hollow shells). This would be explained by a dilution effect due to an unpolarised emission component from within the shells.

Here, we present high signal-to-noise ratio 17 μm diffraction limited images. After deconvolution, the image yields a processed image with a resolution of 0.5 arcsec FWHM.

Sect. 2 describes the observations and the data processing. Sect. 3 presents the derived photometry and the analysis of the structures seen at 17 μm, using as a comparison base, the visible

Send offprint requests to: E. Pantin (epantin@cea.fr)

⋆ Based on data taken at 3.6m telescope, La Silla, ESO, Chile

HST image of the nebula. Sect. 4 presents physical quantities of the dust derived from our data, and finally, Sect. 5 describes the radial structure of the lobes derived from the observations and fits by models of the radial dust density. In particular, we show that the SE lobe, and probably by extension the NW one, have a complex onion-like 3-dimensional structure with a main external shell relatively thick (a fourth of the lobe radius) contrary to the conclusions of Meaburn et al. (1993) who find that the lobes are cavities. Furthermore, we point out the existence of an internal sub-shell centered on 0.4 times the lobe radius. This sub-shell is a possible remnant of a later eruption than the one of 1837–47 or may result from non-uniform deceleration of ejected material during the Great Eruption of 1837–47.

2. Observations and data reduction

We used the mid-infrared camera TIMMI (Thermal Multi-Mode Instrument) mounted on the 3.6m telescope at ESO, Chile (Lagage et al. 1993) to observe η Carinae during July 1997. We observed η Carinae using the N-band filter centered on 10.1 μm ($\Delta\lambda$ = 5.1 μm) and a narrow Q-band filter centered on 17.15 μm ($\Delta\lambda$ = 1.5 μm). The pixel scale of the 17 μm image was 0.3 arcsec/pixel, and the field of view was 19.2 arcsec. The N-band image has a pixel field of view of 0.66 arcsec/pixel and was used for the purpose of deriving a colour temperature map only. The throw of the chopping secondary mirror was 20 arcsec north-south, large enough to avoid overlaps of the positive and negative beams. The reference stars α Scorpii and β Gruis were used as photometric calibrators and as measures of the Point Spread Function for later deconvolution. The weather conditions were exceptionally good for Q-band observations (very low water-vapor pressure) and the seeing conditions in mid-infrared were good, as checked on the reference star. The observations were performed during day time, and show the feasibility of day-time observations in the mid-infrared range. We could not use any close guiding star, but the object (η Carinae) is bright enough to allow an easy recentering of the elementary images during the data reduction phase. Each elementary image corresponds to an integration time of approximatively 20 s, small enough to neglect any spatial drift of the object in the field during this time (we had to re-center the object in the field every 5 minutes). The images were then re-centered during off-line reduction, using a maximum correlation technique well suited to this kind of extended object. The resulting N-band and 17 μm images have photometric errors of less than 8%. The signal-to-noise ratio in both bands varies from more than 300 at the center, to 10 on the edges of the nebula. We did not apply any special signal-processing to the N-band image except shift-and-add. This image was recorded for the purpose of computing a colour temperature map and is not shown in the present paper since it does not bring anything new by comparison with the results of Smith et al. (1995) who already showed a deconvolved 12.5 μm images with a best resolution of 0.35 arcsec. Fig. 1 shows the raw 17 μm image. Fig. 2 shows the resulting deconvolved image at 17 μm. We used the Multiscale Maximum Entropy method (see Pantin & Starck 1996) to deconvolve the raw 17 μm image using β Gru images as experimental Point Spread Function. The final resolution achieved is $\approx$ 0.5 arcsec FWHM. The drawbacks of this method is that very faint structures (several times below the noise level) may disappear in the final deconvolved image. On the other hand, every structure seen in the deconvolved image can be considered as real with a very high degree of probability. Indeed, the use of wavelets decomposition followed by regularized thresholding in the process of deconvolution allows one to compute a final likehood of any structure detected. All the structures seen in Fig. 2 have a probability of being real greater than 99%. Consequently, the two bulges seen at the SW edge of the nebulae (and not seen in 12.5 μm image of Smith et al. 1995) are real with a 99% confidence level.

Table 1. Astrometry of the brightest points seen at 17 μm.

$F_{\nu\ 17.15\ \mu m}$ Jy/"^{2})	loc/*	Comment	Dist. to star (")
2210.7 $\pm$ 176	NE	brightest point	1.8
2082.8 $\pm$ 166	N	second brightest point	0.5
969.8 $\pm$ 77	E	mid-ring joining brightest point to south ring	2.0
500 $\pm$ 40	W	W part of the ring	2.0

3. Photometry and morphology of the Homunculus

3.1. Photometry

Using α Scorpii and β Gruis as standard stars, we derived the photometry at 17.15 μm of the η Carinae nebula to better than 8% accuracy. The total flux of the nebula is $5.61\ 10^4 \pm 4500$ Jy at 17.15 μm. The maximum surface brightness is 2210 Jy/arcsec^2 and is located 1.40 arcsec NE from the apparent location of the central star. If we compare our 17 μm deconvolved image with the 12.5 μm deconvolved image of Smith et al. (1995), we notice that the arc-like structures in the center of the nebula have roughly the same shape. However, the maximum of intensity at 17 μm is not located on the same structure (of the 12.5 μm image), as pointed-out already by Smith et al. (1995). Indeed, the brightest structure at 17 μm is only the second brightest one at 12.5 μm.

3.2. Morphology of the 17 μm image

Fig. 2 displays the 17 μm image with contour added, whereas Fig. 3 shows an WFPC2/HST (June 1995) image through a [F658N] narrow band filter taken from the HST data archive, on which we superimposed the 17 μm image contours. The 17 μm image was visually recentered with respect to the HST image. Those figures display the same coordinate grid and same contour plot.

The global morphology of the nebula at 17 μm matches well the global morphology as given by any recent HST image, *i.e* two gigantic lobes along a NW-SE axis and several small bumps in the NE-SW direction corresponding to equatorial structures. The main differences are in the complex central region where

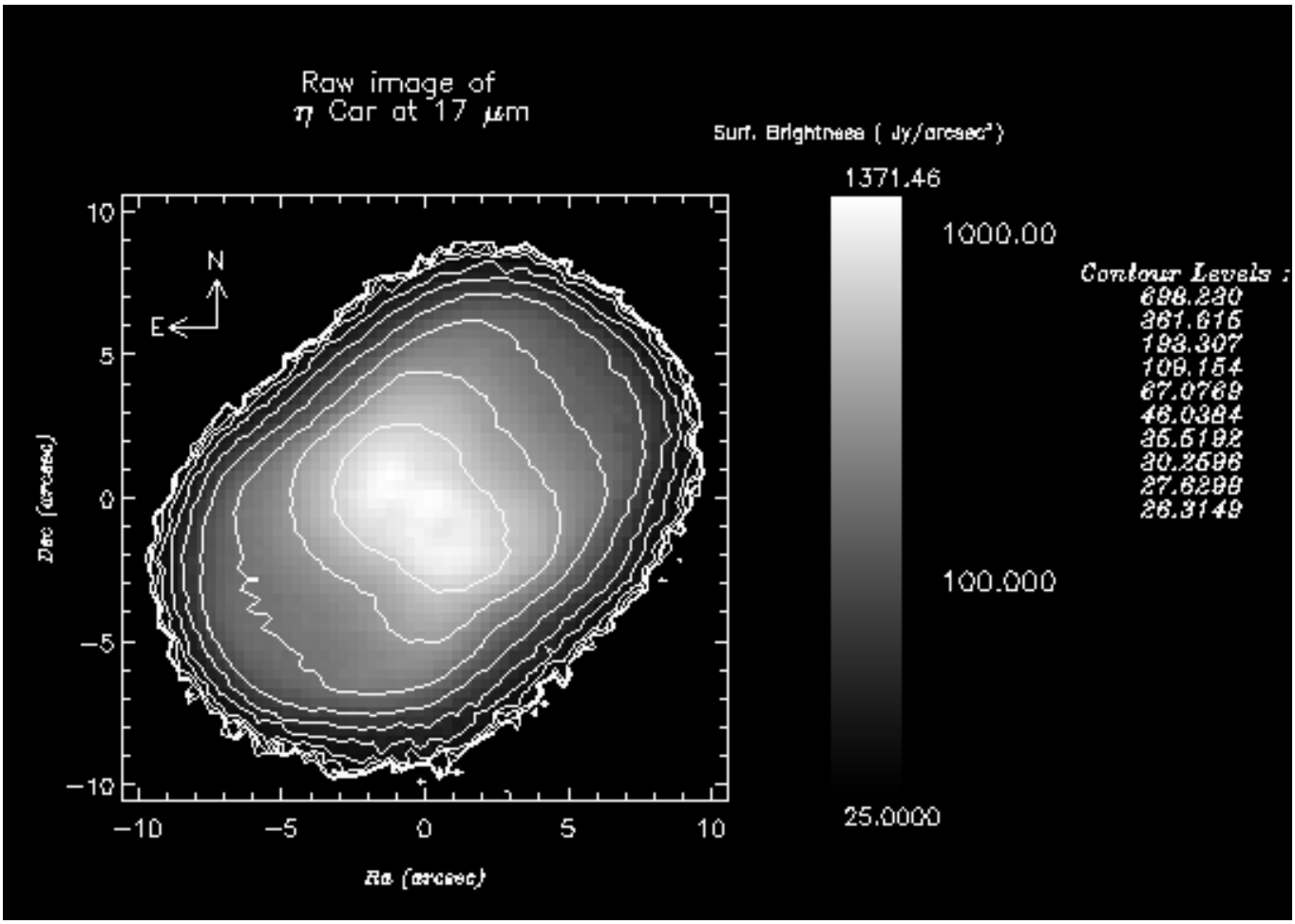

Fig. 1. 17 μm raw image of the η Carinae nebula. The pixel scale is 0.3″/pixel. We have superimposed a grid of contours. At each subsequent contour, the surface brightness is divided by 2. The (0,0) reference position corresponds to the maximum of flux as observed by the HST in the visible range, assumed to be the location of the central star(s).

the maximum location is different: the brightest knot at 17 μm does not correspond to the η Carinae central stellar core (which is the intensity maximum for any image in the optical range), but is located 1.4″ NE from it. The second brightest 17 μm core does correspond to the central optical brightest object. Note that diffraction limited images at 17 μm using a 3.60 m sized telescope does not allow resolution of the $0.5'' \times 0.5''$ inner optical core of η Carinae.

Excluding this very complex central part of the nebula seen in our image, the 17 μm image reveals evidences for point symmetry characteristics rather than axis symmetry. The symmetry center would correspond to the optical stellar core located at the central position (0, 0) in the 17 μm image. The features revealing point symmetry characteristics are the followings (offset position is given in arcsec with respect to the center position):

- the central rectangle area with a mean intensity of $\approx$ 400 Jy/arcsec^{-2} is well centered on (0,0)
- the intensity distribution in the SE and in the NW lobe shows central symmetry features: the horn-like feature, better seen with the contour map at (-2,-6) in the SE lobe, is seen in the opposite lobe at (2,6) and the faintest emissive part in the lobes are located at (-7,-2) for the SE lobe and (7,3) for the NW lobe
- the equatorial "bump" seen in the NE part (-3,4) in the image has its counterpart in the SW of the nebula (3,-4).

The central part of the nebula shows a more complex structure different from the optical image: several bright knots within the central 2.5″ are distributed over two ring-like structures. Those rings are not completely symmetric with respect to the central stellar core but the geometry and the fact that these structures are not proeminent in 12.5 μm images suggest a cold, dense, ring-like structure seen edge-on. Since, we are integrating the signal along the line of sight, and in absence of accurate mid-infrared spectra of the central region it is rather difficult to interpret correctly these complex ring-like structures. For instance, another interpretation could be that the 17 μm maximum intensity region might be a consequence of an overlap of the two lobes that produces an higher emission along the line of sight; it might be also due to density enhancement of dust close to and heated by the central object. Other types (spectra,

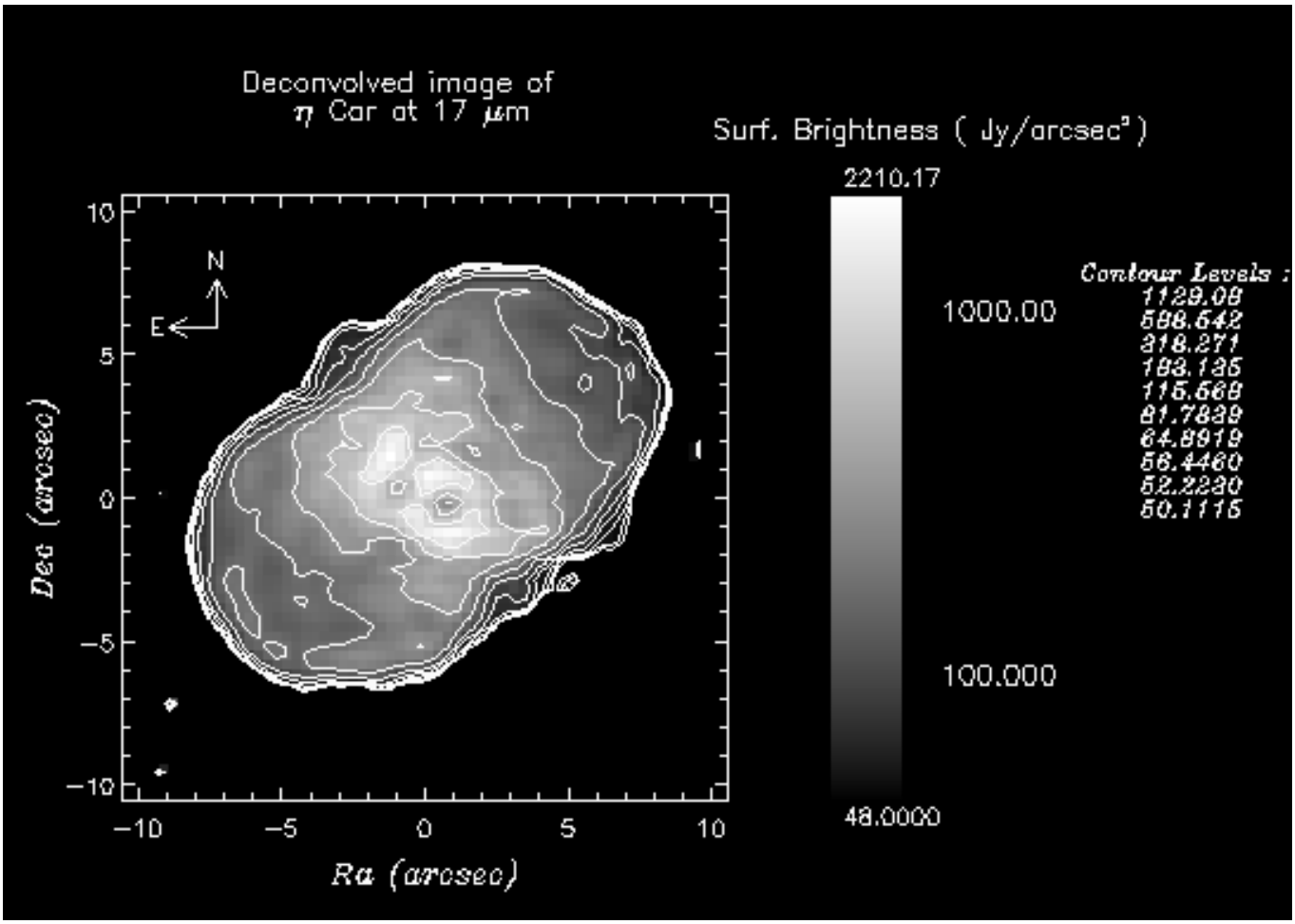

Fig. 2. 17 μm deconvolved image of the η Carinae nebula. The pixel scale is 0.3″/pixel. We have superimposed a grid of contours. At each subsequent contour, the surface brightness is divided by 2. The (0,0) reference position corresponds to the maximum of flux as observed by the HST in the visible range, assumed to be the location of the central star(s).

high-resolution near-infrared images, millimeter scans) of observations are needed to get a clear sketch of the geometry of this zone.

Still, it is interesting to compare the central regions of Smith et al. (1995) 12.5 μm image (Fig. 5 or Fig. 6) with those in our 17 μm image. The equatorial region of the 12.5 μm image of Smith et al. (1995) reveals a NE part brighter than the SW part: the NE equatorial bump is seen whereas nothing appears on the SW symmetric part. Structures located on the NE side of the stellar core are twice as bright as structures on the SW side. The situation is different in our 17 μm image even if the intensity maximum is located on the NE side of the stellar core. Our image does show both NE and SW equatorial bumps and shows that structures located on the SW side of the stellar core are comparable in brightness to the NE ones. Moreover, our column density map (see Fig. 5) shows that the densest regions ($\approx 2.\ 10^{12}$ particles.m^{-2}) are mostly located in the SW region of the stellar core. This column density map is in very good agreement with the emission optical depth map of Hackwell et al. (1986) (Fig. 11). So, we believe the differences between 12.5 μm and 17 μm images come from the fact that the nebula is still not transparent at 12.5 μm in the equatorial regions.

The comparison between the optical HST and 17 μm TIMMI images shows that the "streamers" and other known equatorial features seen superimposed on the NW lobe in the optical images are not clearly seen here. On the other hand, subtle equatorial structures, not superimposed on the lobes, are revealed with TIMMI at a level of $\approx$ 90 Jy/arcsec^2 for the NE and SW "symmetric bumps" and at $\approx$ 55 Jy/arcsec^2 for the faintest one at about (5,-3). Some of those structures coincide well with the η Carinae equatorial skirt structures seen in the HST image like the NE one at (-3,4), the SW one at (6,-2) or the fainter one at (5,-3). On the other hand, the bump at (3,-4) well revealed in the TIMMI image is not seen at all in the HST image. We think that dust extinction hide this SW bump at visible wavelengths since it is close to the SW equatorial regions where we see an increase in the column density (see Fig. 5).

Since the internal part (excluding the lobes) of the nebula is difficult to interpret because of a sum of projection effects, we concentrate on the lobes for the modeling of the structure.

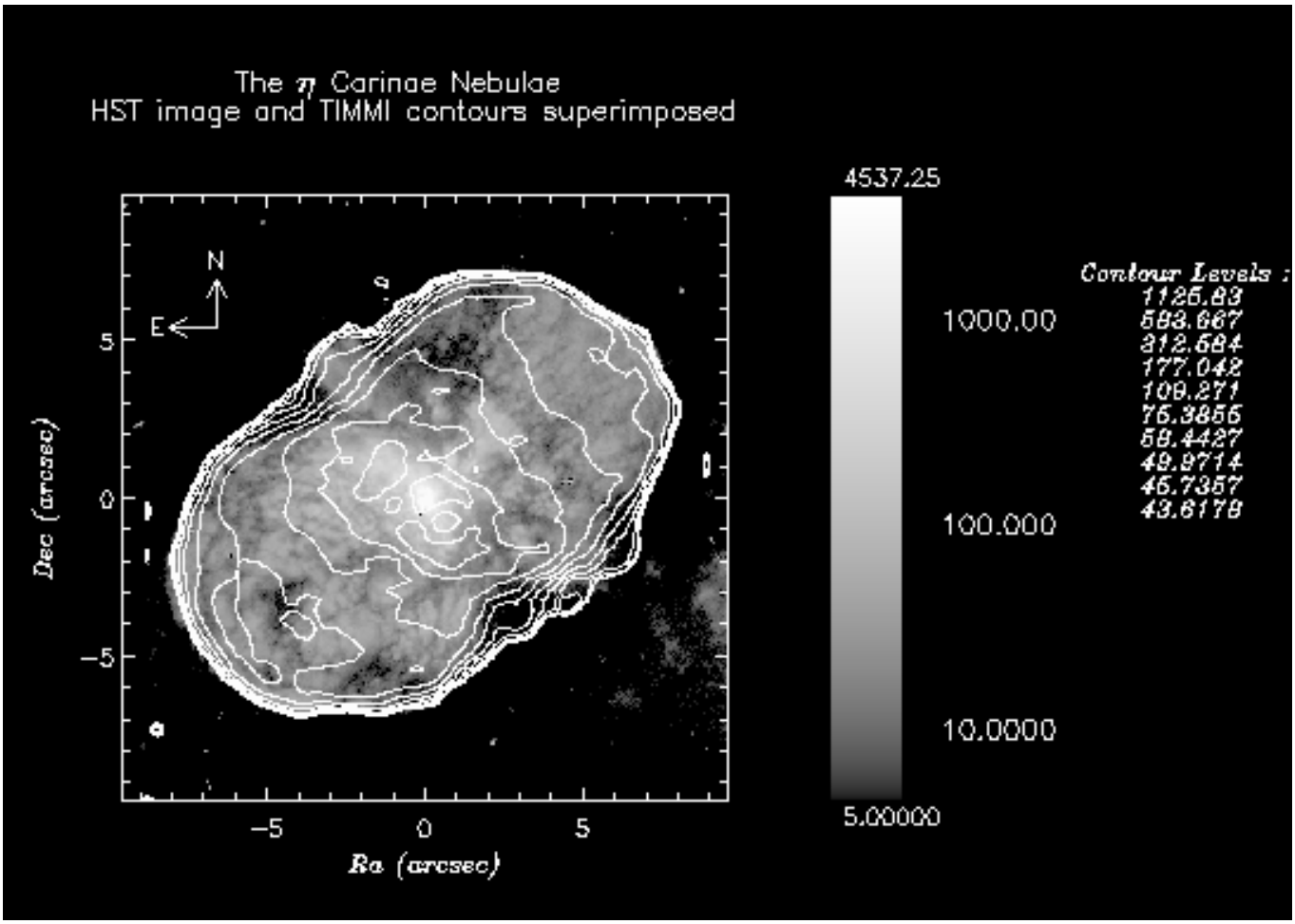

Fig. 3. Comparison of the structures seen at 17 μm and in the visible, with the HST. We have superimposed the TIMMI 17 μm contours to the WPC2/HST [F658N] image.

4. Some physical quantities of the dust derived from our data

In building the thermal emission model of the dust in the lobes, we assumed that the dust particles are composed essentially of Draine & Lee (Draine & Lee 1984; Draine 1985) astronomical silicate grains, based on the fact that the 10 μm spectrum shows the signature of amorphous silicates (Robinson et al. 1987). We took a canonical size distribution following a power-law with an index of -3.5 (cf Dohnanyi 1969; Mathis et al. 1977). The grain sizes are ranging from 0.1 to 2 μm (Smith et al. 1995) resulting in a final mean size of 0.15 μm, compatible with the results of Robinson et al. (1987) and the knowledge we have about the typical sizes of freshly synthetized dust grains.

From the (non-deconvolved) N-band and smoothed 17 μm images (in order to have a 17 μm image having the same resolution as the N-band image), we could derive a mean colour temperature map in the lobes of the nebula. The somewhat low resolution of this map (around 1.2 arcsec) is not really a problem since the temperature should be a physical quantity that varies smoothly inside the lobes. The **colour temperature** shown in Fig. 4 varies from 350 K in the central part of the nebula to 190 K on the edges of the lobes. As pointed out in many previous works, the characteristic temperature of the lobes is in the range 200–220 K (e.g. see Cox et al. 1995). The colour temperature map reveals a region extending 3 arcsec towards the E-SE direction superimposed on the SE lobe that has higher temperature in the 300–350 K range. We also observe a similar feature at a temperature of about 270 K for an area projected over the NW lobe extending towards W-NW. The temperature map of Hackwell et al. (1986) (Fig. 11c) shows similar extended areas having similar temperature (between 250 and 350 K) projected over the same regions. Some investigators infer the presence of other types of dust, like corundum (aluminum oxide) (Mitchell & Robinson 1978) or iron (Mitchell & Robinson 1986). Replacing the silicate dust by these other types would not modify significantly the colour temperature map. We found also that the derived temperatures do not change significantly if one changes the cut-off sizes of the dust grains or the index of the size distribution power-law.

The physical quantities we derived from this study are the following. Assuming a distance to η Carinae of 2.2 kpc (Allen & Hillier 1993), the total mass of dust in the nebula is 0.02 $M_{\odot}$,

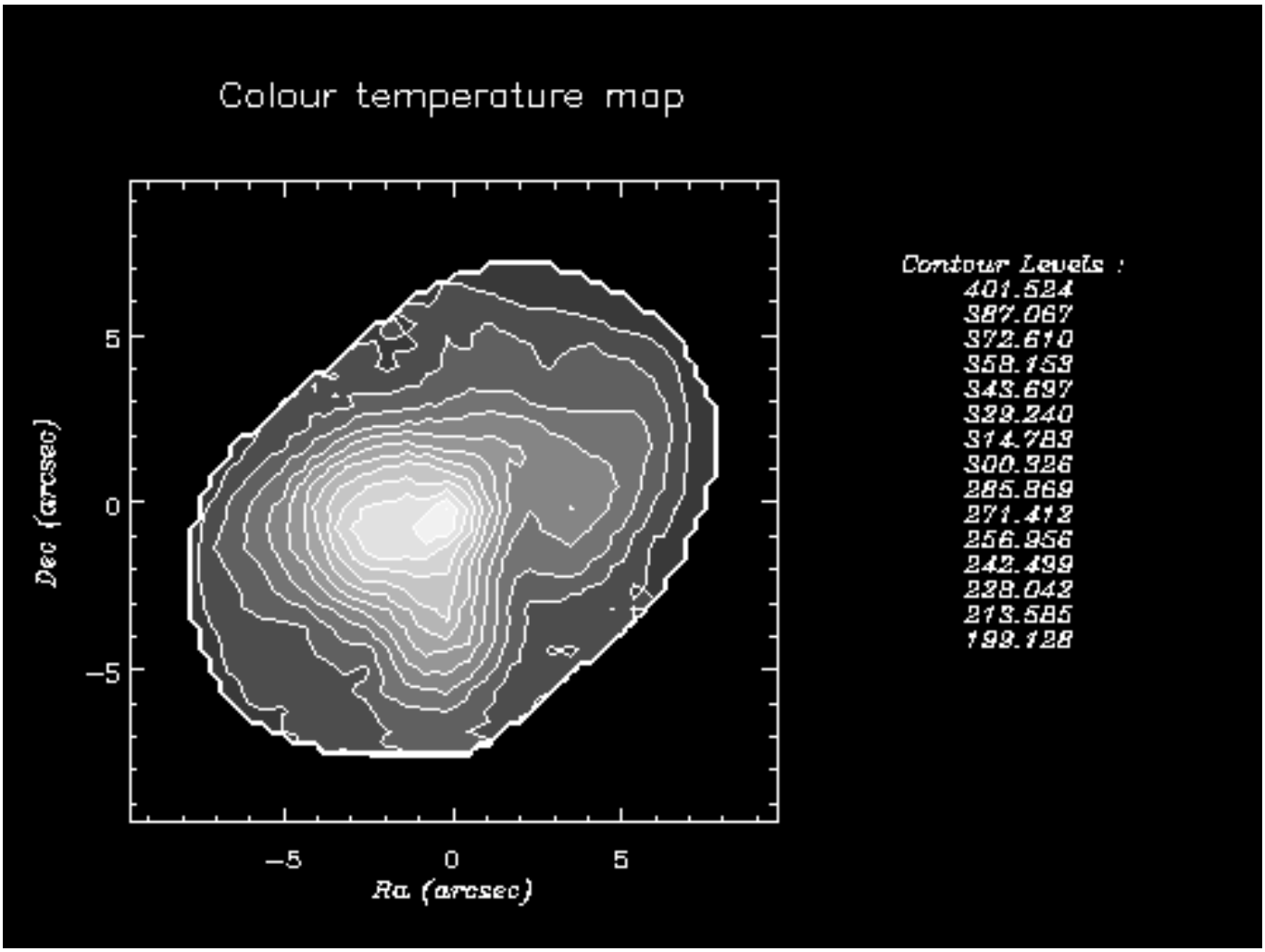

Fig. 4. Colour temperature map of the η Carinae nebula, derived from the (non-deconvolved) N-band and smoothed 17 μm image.

implying a total mass of $\approx 2\ M_\odot$ when assuming a canonical gas to dust mass ratio of 100. The total dust mass is in agreement with the result of Hackwell et al. (1986) who derived a total dust mass of 0.012 $M_\odot$ from deconvolved data and Mitchell & Robinson (1978) who found a total dust mass of 0.03 $M_\odot$. We found that the column densities of dust in the lobes, derived from 17 μm images (a wavelength at which the lobes are thought to be optically thin) span from a value of $4.2\ 10^{11}$ particles.m^{-2} at the center of the lobes to a value in the range 8.4–$12.6\ 10^{11}$ particles.m^{-2} on the edges (see Fig. 5). The corresponding optical depths at 17.15 μm are τ = 0.002 and 0.015 respectively. The emission optical depth map of Hackwell et al. (1986) at 9.7 μm, reveals values greater than unity for the same regions.

5. Structure of the lobes as revealed by the column density map

Using the temperature map and the deconvolved 17 μm image, we derived a map of dust column density in the lobes. The method used to derive this dust column density map is described in Appendix 1. The column density map is shown in Fig. 5. Firstly, one can notice very clumpy structures of the dust in the innermost regions of the nebula. Secondly, there is an increase in the density from the center of the SE lobe to its edges. The NW lobe shows a similar structure on it SW side, but has a different, more complex, shape in its northern part (as already mentioned by Allen & Hillier 1993). We attribute this to a projection effect, since the nebula is supposed to have an axis that is inclined 40 degrees from the plane of the sky (Meaburn et al. 1987) so that the NW lobe is partly hidden by the disk-like structure seen on HST images. Therefore, we examined the radial density of the SE lobe only. In the following, the term radius refers to a spherical system of coordinates centered indifferently on the center of the SE lobe or the NW lobe depending on the lobe we refer to in the sentence (but in general we refer to the SE one, since we concentrated our study on this lobe). At a first order, we consider the two lobes as spherical shells aligned along an axis oriented PA 132° and we plot (see Fig. 6) the dust column density along three position angles (perpendicular to the main axis) represented on the column density map (see Fig. 5). Any cut through the central part of the southern lobe (like the upper plot in Fig. 6 corresponding to position #2 in Fig. 5) presents

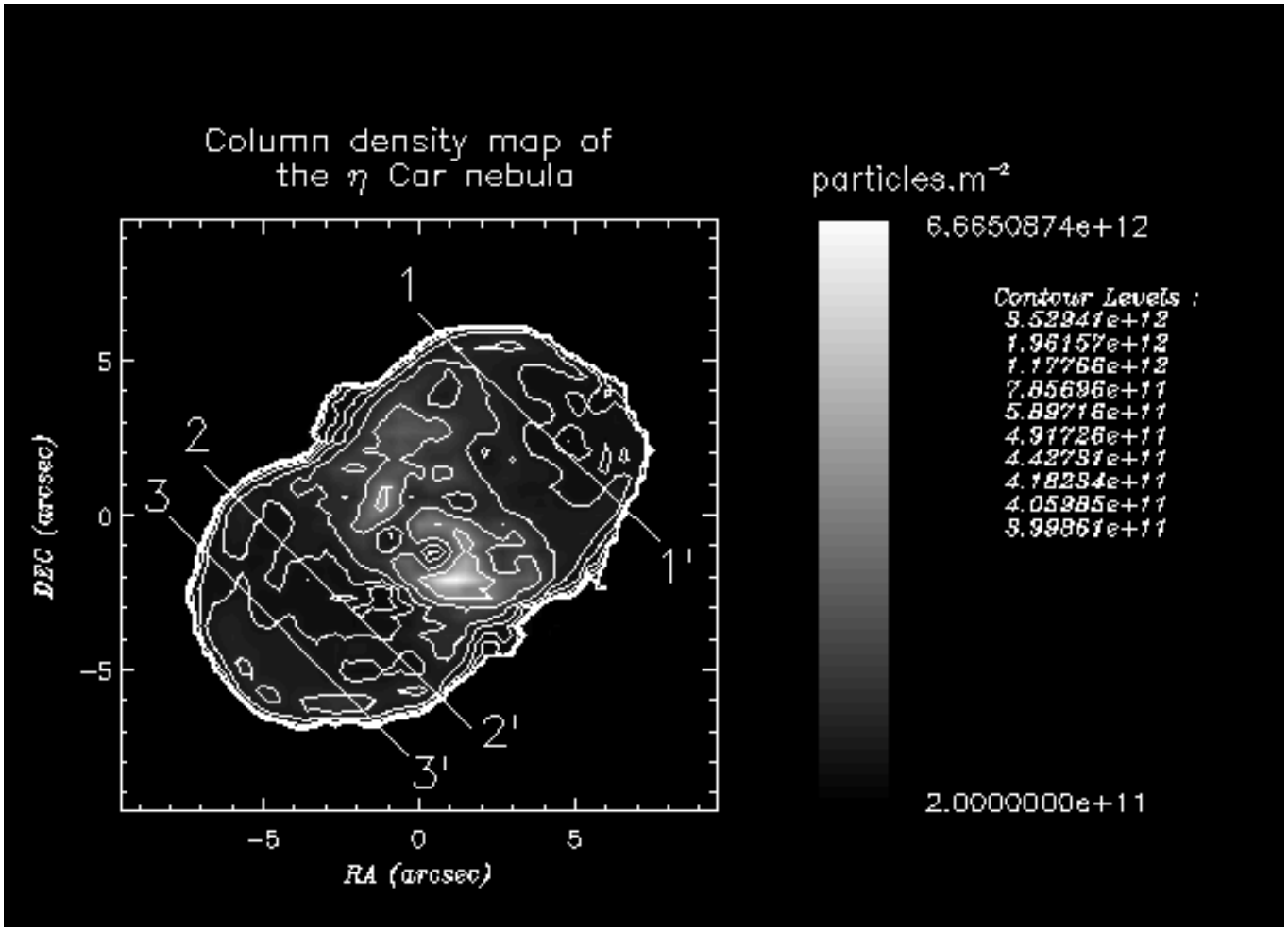

Fig. 5. Column density map of the η Carinae nebula, pixel scale is 0.3″/pixel and represents 660 AU at the distance of η Carinae. Superimposed are lines numbered 1 to 3 showing the position angles for the profiles shown in Fig. 6

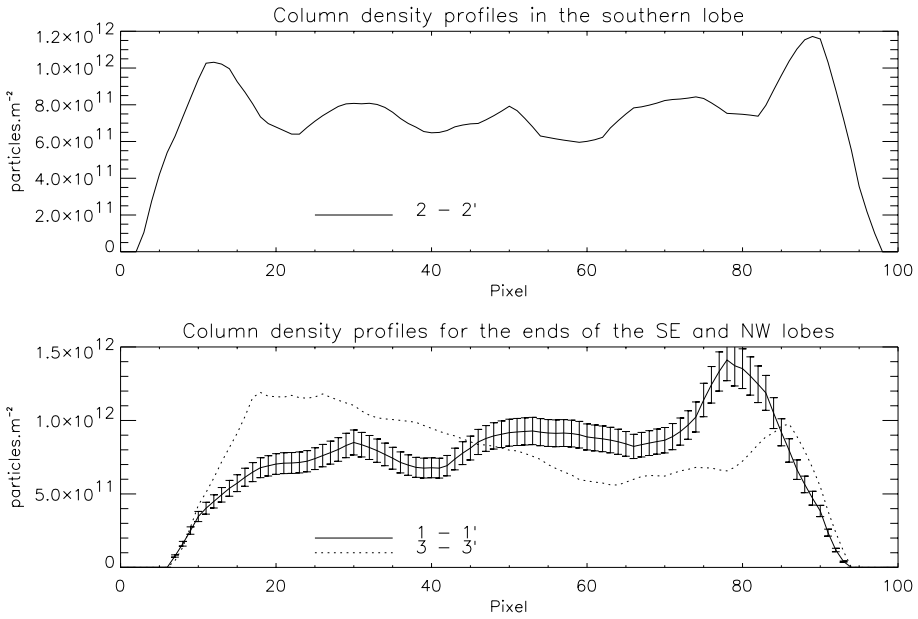

Fig. 6. Profiles for different positions in the column density map as labeled in Fig. 5. Error bars are of 10% value, but have been included only for profile #3 for purposes of clarity. Note the symmetrical, wave-like feature in the upper figure and the increase in column density westward and eastward respectively for the southern and northern lobe edges.

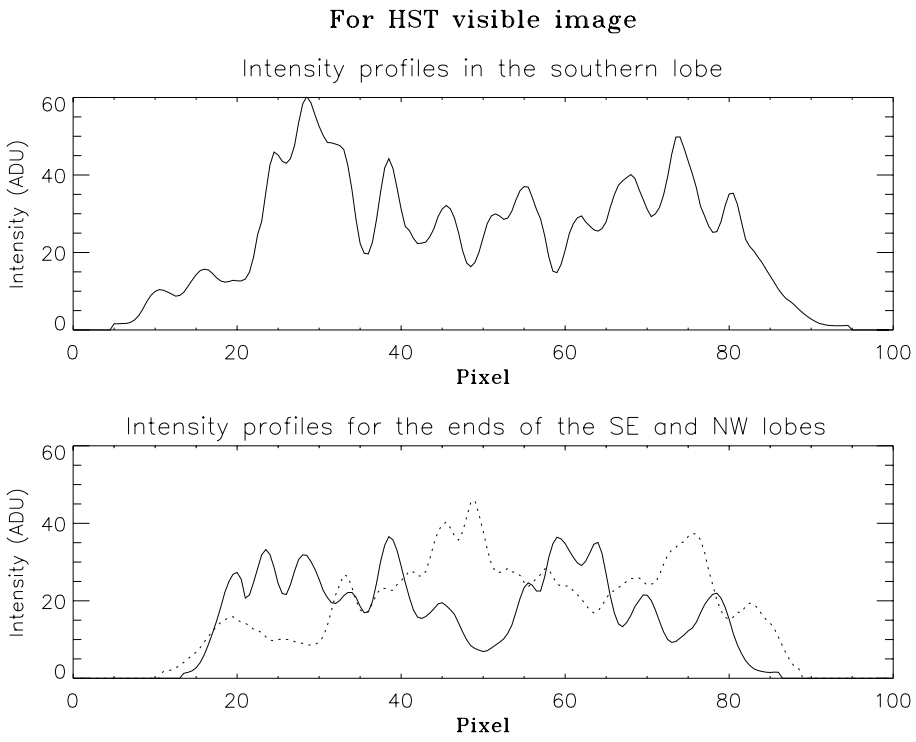

Fig. 7. Intensity profiles for the HST visible image for the position angles as given and labeled in Fig. 5. Note that there is no correlation between those intensity variations attributed to the lobe surface clumpiness and the variations in the column density profiles given in Fig. 6.

a similar shape, *i.e* an external maximum of column density on the edges, a minimum around 0.65 times the lobe radius, a second maximum around 0.4 radii, a second minimum around 0.2 radii, and a third maximum at the center of the lobe. Those dust column density variations are well above the error bars.

To check whether this finding was not simply due to the clumpiness that appears on the lobe surface in the HST visible image, we extracted the intensity profile for the same position angles from the HST image. The plots shown in Fig. 7 reveal that there is no correlation between those clumpiness and the column density profiles. The column density variations are really the consequence of density enhancements along the line of sight trough the lobe.

The lobes appear not to be simply hollow structures, but are three dimensional onion-like structures with a thick, dense, external shell as we demonstrate it in the next section.

We assumed that the 17 μm emission in the lobes is strictly optically thin (checked by a value of $\tau \ll 1$). We have then an "X-ray like" picture of the lobes from which one can derive the radial function of dust density. We had to assume a geometry for the lobes since we have only one projection coming from a single line-of-sight angle (from two independent angles, one could avoid any assumption on the geometry and the problem would be considered as a tomography inverse problem). We concentrated then on the SE lobe which represents the simplest case because it is not affected by projection effects from the equatorial skirt.

In order to have access to the radial structure of the lobes and try to interpret our 17 μm data, we built a simple model. In this model, we assumed that the SE lobe has a spherical structure (simplest assumption) and we tried to find the corresponding function of radial density. We started with a first guess for the radial density (one single external shell), we projected this function and compared the projection to our data (profile #2 of the column density map, Fig. 5). Then, we modified the radial density taking into account the discrepancies between data and model and we iterated the process until we got a satisfactory fit of the data, compatible with the errors. Our best model is represented in Fig. 8 and Fig. 9. One distinguishes three different maxima of density corresponding to three shell-like features. However, as shown on the cumulative material plot on Fig. 8, the majority of the lobes material is essentially contained in the outer thick shell. We found that the density of the grains is ranging from $2.\ 10^{-5}$ part.m^{-3} within the lobe to a maximum of $8.\ 10^{-4}$ part.m^{-3} in the outer shell, leading to a total number of dust particles of $4.\ 10^{42}$ for one lobe. Assuming a lobe radius of 9 500 AU (corresponding to 8.5 arcsec for the lobe diameter at a distance of 2200 pc), the inner shell extends from the center to more than 950 AU; the secondary shell starting at about 0.3 radius (2 850 AU) extends over more than 2 160 AU; finally, the outer shell starts at 0.7 radius (6 650 AU) and extends over more than 2 850 AU.

According to our model, the outer shell contains about 90% of the total amount of material contained in the lobe (see Fig. 8). The external shell could be attributed to the major eruption from 1837–1847. The other local maxima of radial density may come from non-uniform deceleration of material in the lobes, or from later eruptions. As reviewed by Viotti (1995), different increases in brightness occurred after the Great Eruption from 1843: a first one is mentioned in 1860–1862, a second around 1870 and a later one corresponding to the Lesser Eruption in 1887–1892 with a remarkable five year permanence at maximum luminos-

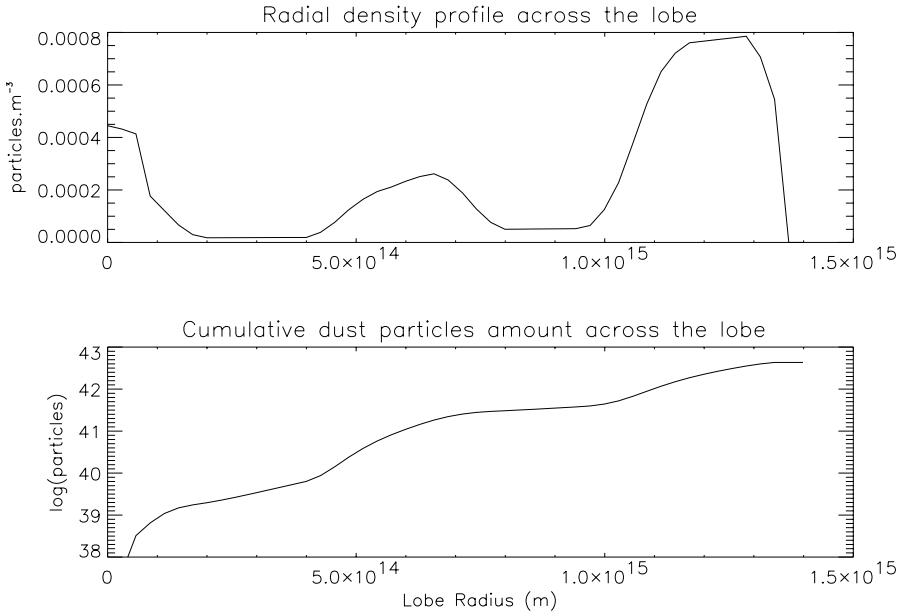

Fig. 8. Top: Best model for the radial density distribution as a function of lobe radius, best fitting to the projected density for position #2 (see also Fig. 9). Bottom: cumulated material in the lobe as a function of the lobe radius.

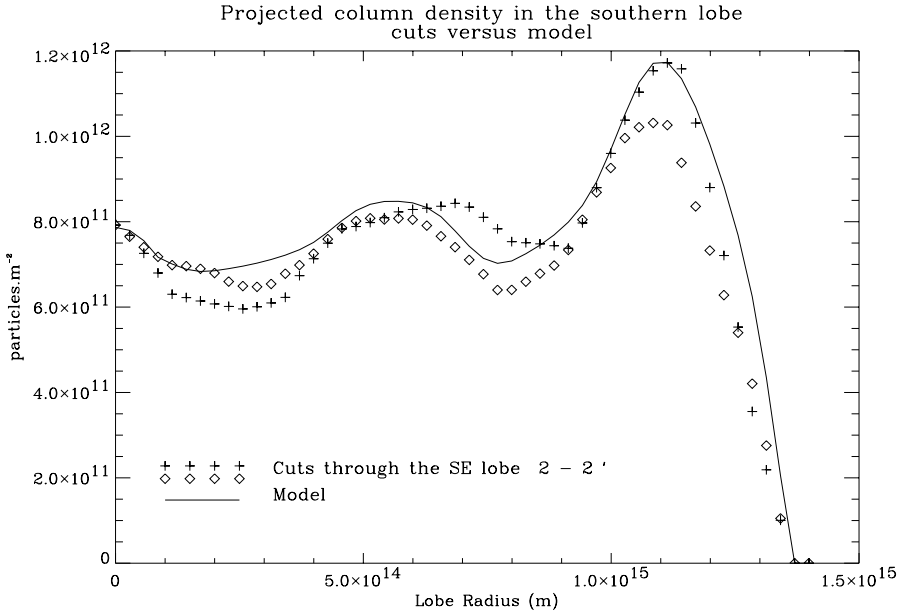

Fig. 9. Projection of the radial profile from Fig. 8, Overplotted are the observed cut through the SE lobe along the line marked #2 as a function of the apparent lobe radius.

ity. Since we do not have any velocity field information for the inner shells, it would be hazardous to try to associate the inner shells with the historical light maxima.

Finally, as seen in the column density map of Fig. 5, the NW and SE edges of the nebula does not present any maximum of column density i.e the column density values, when following the lobes edges from position 1 to position 1′ for the NW lobes, and from position 3 to position 3′ for the NW lobes, do not show any geometrically significant variations (less than 20%). A non spherical model like the double-flasks model proposed by Currie et al. (1996a) would produce a significant increase of density around the crossing point of the nebulae axis and the edge of the lobes. Since we do not see such an increase of density within a factor of 20%, our observations tend to reject this double-flasks model.

6. Conclusion

We have presented a new deconvolved 17 μm image of the η Carinae nebula which has a signal-to-noise ratio never reached before. We obtained an accurate 2-D photometry map at 17 μm of the object, with a precision of 8%. We compared the structures seen at 17 μm with those observed in the visible range by the HST, and pointed out that the maximum of emission in the visible range and at 17 μm are not correlated. Using simultaneous N-band images and a thermal dust model, we derived a temperature map for the lobes and then derived the column density in the lobes. We discovered that the internal structure of the lobes is more complex than first thought, showing clumps and local density maxima (sub-shell). We could find a radial density profile able to match the projected column density. This radial

density shows that inner structure of the lobes is composed of a large thick external shell plus a higher density region between a distance of 3500 and 6500 AU from the center of the lobe. This secondary shell could be formed during a later and weaker eruption after the main one of 1837–47 (maybe the Lesser one of 1890?). The physics of the ejection mechanism should be better constrained if we could get a precise idea of the 3-D structure of the lobes. The results presented here try to partially answer this question. However, many questions remain regarding this intriguing object and its surrounding nebula, like, for instance, the exact composition of the dust in the nebula and the nature of the central object.

Acknowledgements. WFPC2 images of η Carinae are based on observations made with the NASA/ESA Hubble Space Telescope, obtained from the data archive at the Space Telescope Science Institute. STScI is operated by the Association of Universities for Research in Astronomy, Inc. under the NASA contract NAS 5-26555. We would like to thank our referee Dr. C. Wright for his careful reading of the original version of this paper and for his suggestions for its improvement. EP wishes to thank the Katholieke Universiteit of Leuven for a fellowship. DLM thanks the European Southern Observatory for a studentship.

Appendix A: derivation of the column density map

Starting from non-deconvolved N band and 17 μm images, one can derive a temperature map by the following procedure:

In the following we assume the 17 μm emission to be optically thin in the lobes, and that the lobes are spherically symmetrical. We already see in the deconvolved 17 μm image that there is an enhancement of flux on the edges of the bipolar lobes. From this fact and also from the results of anterior works, we can assume as a first approximation that the lobes are hollow and that on a given pixel, the dust has a constant temperature $\langle \mathrm{T} \rangle$ (the temperature of the dust on the edge of the lobes which dominate the infrared flux) given by the resolution of the following expression:

$$\frac{F_{17}}{F_{10}} = \frac{\int \pi a^2 Q_{abs}(17\,\mu m, a) B_\nu(17\,\mu m, \langle T \rangle) n(a) da}{\int \pi a^2 Q_{abs}(10\,\mu m, a) B_\nu(10\,\mu m, \langle T \rangle) n(a) da} \quad \text{(A.1)}$$

The absorption coefficients Q_{abs} are obtained by applying Mie theory to Draine & Lee (1984) astronomical silicates, using optical constants from Draine (1985). In Eq. (1) the size of the spherical grain is denoted by a, whilst N(a)da is the size distribution of the grains that follows a power-law with index -3.5 between the minimum size (0.1 μm) and the maximum size (2 μm), and is equal to 0 outside the cut-off sizes.

From the temperature map, the first guess of the column density for each pixel is obtained by:

$$n = \frac{F_{17}}{\int \pi a^2 Q_{abs}(17\,\mu m, a) B_\nu(17\,\mu m, \langle T \rangle) n(a) da} \quad \text{(A.2)}$$

We then apply the "deprojection" procedure described in Sect. 5 in order to deduce from the column density a first guess of the radial dust density distribution. Since this first guess does not take into account the change of dust temperature when going from the edges to the center of the lobe, we apply to the radial density a correction function inversely proportional to the variation of thermal flux from the edges to the center of the lobe.

This function is given by:

$$f(r) = \frac{e^{\frac{h\nu}{kT(r)}} - 1}{e^{\frac{h\nu}{k\langle T \rangle_e}} - 1} \quad \text{(A.3)}$$

where $\langle \mathrm{T} \rangle_e$ is the temperature on the edge at a distance of $\sqrt{2}$ lobe radii from the central source, and measured on the temprature map.

The inner lobe mean temperature of the grains (averaged on the sizes on the grains) can be computed assuming thermal equilibrium of the grains heated by a central source. Assuming that the grains are good absorbers (in the UV/visible) and emit in the infrared inefficiently (which is indeed the case for grains in the range 0.1–2 μm), it can be shown that the temperature dependence with the distance to the central source follows a power-law with -2/5 index (Backman & Paresce 1993). Then, we have:

$$T(r) = \langle T \rangle_e \left(\frac{r}{\sqrt{2}R} \right)^{\frac{-2}{5}} \quad \text{(A.4)}$$

where R is the lobe radius.

References

Aitken D.K., Smith C.H., Moore T. J.T, Roche P.F., 1995, MNRAS 273, 359
Allen D.A., Hillier D.J., 1993, Proc. Astr. Soc. Austr. 10, 338
Backman D.E., Paresce F.C., 1993, in *Protostars and Planets III*, eds. Levy E.H., Lumine J.I., Matthews M.S., Univ. Arizona Press, Tucson, 208.
Cox P., Mezger P.G., Sievers A., et al., 1995, A&A 297, 168
Currie D.G., Dowling D.M., Shaya E.J., Hester J.J, The HST WF/PC Instrument Definition Team, and the HST WFPC2 Instrument Definition Team, 1996a, in *The role of dust in the formation of stars*, ESO workshop, H.U. Kaufl and R. Siebenmorgen eds., p. 89
Currie D.G., Dowling D.M., Shaya E.J., et al., 1996b, AJ 112, 1115
Davidson K., Ebbets D., Johansson S., et al., 1997, AJ 113,335
Dohnanyi J., 1969, J. Geophys. Res 74, 2531
Draine B.T., 1985, ApJS 57, 587
Draine B.T., Lee H.M., 1984, ApJ 285, 89
Gaviola E., 1950, ApJ 111, 408
Hackwell J.A., Gehrz R., Grasdalen G.R., 1986., ApJ 311, 380
Lagage P.O., Jouan R., Masse P., et al., 1993, in *Infrared Detectors and Instrumentation*, (Fowler, A.W. Ed.), Vol. 1946, 655 (SPIE publisher, 1993).
Mathis J.S., Rumpl W., Nordsieck K.H., 1977, ApJ 217, 425
Meaburn J., Wolstencroft R.D., Walsh J.R., 1987, A&A 181, 333
Meaburn J., Walsh J.R., Wolstencroft R.D. 1993, A&A 268, 283
Mitchell R.M., Robinson G., 1978, ApJ, 220, 841
Mitchell R.M., Robinson G., 1986, MNRAS 222, 347
Pantin E., Starck J.L., 1996, A&AS 118, 575
Rigaut F., Gehring G. 1995, Rev. Mex. Astron. Astrofis. 2, 27
Robinson G., Mitchell R.M., Aitken D.K., et al., 1987, MNRAS 227, 535
Smith C.H., Aitken D.K., Moore T.J.T., et al., 1995, MNRAS 273, 354
Viotti R., 1995, Rev. Mex. Astron. Astrofis. 2, 10